Long term variation of aerosols lidar ratio in Shanghai based on Raman lidar measurement

Tongqiang Liu[1], Qianshan He[2, 3,*], Yonghang Chen[1,*], Jie Liu[2], Qiong Liu[1], Wei Gao[2], Guan Huang[1], Wenhao Shi[1], Xiaohong Yu[4]

[1]College of Environmental Science and Engineering, Donghua University, Shanghai, 201620, China
[2]Shanghai Meteorological Service, Shanghai, 201199, China
[3]Shanghai Key Laboratory of Meteorology and Health, Shanghai, 201199, China
[4]Shanxi Institute of Meteorological Sciences, Taiyuan, 030000, China

Correspondence to: Qianshan He (oxeye75@163.com) and Yonghang Chen (yonghangchen@dhu.edu.cn)

Abstract. Accurate Lidar ratios (LR) and better understanding of their variation characteristics can not only improve the retrieval accuracy of parameters from elastic lidar, but also play an important role in assessing the impacts of aerosols on climate. Using the observational data of Raman lidar in Shanghai from 2017 to 2019, LR at 355 nm were retrieved and their variations and influencing factors were analyzed. Within the height range of 0.5 km–5 km, about 90% of the LR were distributed in 10 sr–80 sr with an average value of 41.0±22.5 sr, and the LR decreased with the increase of height. The volume depolarization ratios (δ) were positively correlated with LR, and they also decreased with the increase of height, indicating that vertical distribution of particle shape was one of the influencing factors of the variations of LR with height. LR had a strong dependence on the original source of the air masses. Affected by the aerosols transported from the northwest, the average LR was the largest, 44.2±24.7 sr, accompanied by the most irregular particle shape. The vertical distributions of LR were affected by atmospheric turbidity, with the greater gradient of LR under clean conditions. The LR above 1km could be more than 80 sr, when Shanghai was affected by biomass burning aerosols.

1 Introduction

The increase of aerosol loadings leads to haze pollution and the decrease of atmospheric visibility (Wang et al., 2010), and also affects the earth's radiation budget and water cycle in various ways (Koren et al., 2004; Twomey, 1977). The knowledge of aerosol vertical distribution and its absorption properties are required to assess the impacts of aerosols on climate change and study the mechanism of air pollution (Ferrare et al., 2001; Sicard et al., 2011).

As an active remote sensing instrument, the elastic scattering lidar can obtain vertical distribution information of aerosols, however, it is necessary to assume aerosol extinction to backscattering ratios (i.e., lidar ratios, LR) in retrieval process (Fernald, 1984; Welton et al., 2001), which can result in significant errors for the extinction coefficient and followed by aerosol optical depth (AOD). To our knowledge, the LR at 355nm, 532nm and 1064nm are usually assumed to be 50 sr in

China (Fan et al., 2018; Gong et al., 2015; Lv et al., 2020; Ma et al., 2019). In addition, the CALIOP (Cloud-Aerosol Lidar with Orthogonal Polarization) onboard the CALIPSO (Cloud-Aerosol Lidar Infrared Pathfinder Satellite Observations) can observe the vertical distribution of global aerosol optical properties, and its data products have been widely used around the world (Kim et al., 2018). The CALIOP algorithm first determines the type of aerosol according to aerosol classification algorithm, and then uses lookup table of multiple types of aerosol to determine the LR (Kim et al., 2018; Omar et al., 2009). Therefore, the quality of the CALIOP aerosol products depends on the accuracy of aerosol type identification and the consistency between actual LR and that in the look-up table (Painemal et al., 2019). LR are complicated functions of time and space, which depend on aerosol size distribution and particle composition (Reagan et al., 1988). LR are also affected by meteorological elements (Salemink et al., 1984), such as relative humidity (RH), which can change aerosol particle size distribution and refractive index (Young et al., 1993). Therefore, good knowledge of accurate LR and their variation characteristics can not only improve the retrieval accuracy of parameters from elastic lidar, but also obtain information on aerosol types to trace the source of pollution (Franke et al., 2001).

According to the definition of LR in Müller's (2003) study:

$$\mathrm{LR}=\frac{4\pi}{\omega P(\pi)} \tag{1}$$

LR was negatively correlated with phase function at 180° ($P(\pi)$) and single-scattering albedo (ω). $P(\pi)$ was related to sphericity of particles, and the sphericity information of particles can be obtained from polarization lidar. ω is indicative of aerosol absorption properties. The aerosol absorption properties and their vertical distributions play a crucial role in evaluating direct radiative forcing of aerosols (McComiskey et al., 2008; Zarzycki and Bond, 2010). Moreover, absorbing aerosols increases atmospheric stability by reducing the solar radiation reaching the surface during the day. On the contrary, absorbing aerosols on near surface layer heats the surface and increases the atmospheric instability during night (Jacobson, 1998; Jacobson and Kaufman, 2006). The vertical profile of LR can reflect vertical variations of aerosol absorption properties, which can provide a basis for studying aerosol radiative forcing and causes of pollution (Mishchenko et al., 2004).

LR can be obtained by a variety of methods, such as high spectrum resolution lidar (HSRL), Raman lidar and joint retrieval using sun photometer and elastic lidar (Zhao et al., 2018). Raman lidar can independently retrieve the extinction coefficient and backscatter coefficient of aerosols and obtain LR by combining elastic backscatter and Raman backscatter signals (Ansmann et al., 1992), which is the most widely used independent measurement method at present. Moreover, the LR measured by Raman lidar are useful indexes to study the variations of aerosol physical properties (Ferrare et al., 2001).

A large number of observations and analyses of LR have been carried out all over the world based on Raman lidar. Since the establishment of the European Aerosol Research Lidar Network (EARLINET) in 2000, a long-time series observation data of vertical distribution and LR for various types of aerosol has been obtained in the European continent (Müller et al., 2007; Wandinger et al., 2016). In South Korea and Japan, some researches have also been carried out on the LR of Asian dust and biomass burning aerosols based on Raman lidar (Murayama et al., 2004; Noh et al., 2007 and 2008).

The LR observed around the world usually show different values due to different types of aerosols. However, long-term observations and researches of LR in China are limited (Wang et al., 2016) due to the limitation of observation instruments. In particular, the observations and studies of aerosol LR are still blank in East China. Generally, range-resolved LR profiles based on independent measurement on a regional scale were very important. On the one hand, the range-resolved LR obtained from ground-based Raman lidar can not only be used to compare with 355nm LR obtained from ATLID (Atmospheric LIDar) on the EarthCARE (Earth Clouds and Radiation Explorer) planned to be launched by ESA (European Space Agency) (Liu et al., 2020; Nicolae et al., 2018), but also can provides a reliable basis for the inversion hypothesis of elastic lidar in Shanghai and surrounding areas, and improves products reliability from elastic lidar network such as the Asian dust and aerosol lidar observation network. On the other hand, vertical distribution of aerosol absorption properties reflected by LR can be used as an input parameter of regional climate models (Mehta et al., 2018), which can further improve calculation accuracy of radiative forcing.

In addition, studying the influencing factors of LR in Shanghai can be conducive to understanding the LR variation characteristics and determining the source of pollutants. With these motivations, the vertical and temporal variations of LR and their influencing factors were analyzed in Shanghai by using the results retrieved from Raman lidar, which laid a solid foundation for quantitative study of pollution variations and its causes in the future.

2 Data and methods

2.1 Observation equipment and data

2.1.1 Raman depolarization lidar

The Raman depolarization lidar (Raymetrics S.A., Athens, Greece, model LR231-D300) used in this study is deployed on a building roof (121.4333°E, 31.1916°N; 67 m above sea level, ASL) in Shanghai downtown. The site is 35 km from the East China Sea coastline, surrounded by populated residential and commercial areas. The laser of the lidar system is Nd: YAG pulse laser equipped with water cooling device. The system can emit 355 nm, 532 nm and 1064 nm laser pulses with a pulse width of 5.4 ns and a repetition rate of 20 Hz. The lidar detection system can receive 355 nm, 532 nm and 1064 nm elastic scattering signals. The 532 nm elastic scattering channel has two polarization channels, 532P (parallel) and 532S (perpendicular). In addition, the lidar can also receive the vibrational Raman scattering signals of nitrogen (387 nm) and water vapor molecules (408 nm) with an incident wavelength of 355 nm. Therefore, the LR obtained and discussed in this study is at 355nm. The transient recorder can detect signals in two modes: analog and photon counting. The analog mode is suitable for detecting strong signals at low altitude, and the photon counting mode is suitable for detecting weak signals at high altitude. In order to better combine the advantages of the two modes to retrieve aerosol optical properties, it is necessary to glue signals of the two modes (Newsom et al., 2009; Walker et al., 2014). The range resolution of the raw signal is 7.5 m,

and the temporal resolutions are 1 min (before January 25, 2019) and 2 mins (after January 25, 2019), respectively. The time in the paper without special explanations was UTC.

2.1.2 HYSPLIT-4

HYSPLIT-4 (Hybrid Single Particle Lagrangian Integrated Trajectory Model, Version 4) is a professional model jointly developed by the National Oceanic and Atmospheric Administration (NOAA) and the Australian Bureau of Meteorology for calculating and analyzing transport and diffusion trajectories of atmospheric pollutants, and has been widely used in many studies around the world (Huang et al., 2012; Noh et al., 2007). It supports the input of a variety of meteorological data, and NOAA reanalysis of meteorological data was used in this study.

2.1.3 MERRA-2

MERRA-2 (The Modern-Era Retrospective Analysis for Research and Applications, Version 2) is an atmospheric reanalysis dataset provided by the National Aeronautics and Space Administration (NASA) and the Global Modeling and Assimilation Office (GMAO) (Gelaro et al., 2017). The aerosol optical property data used in this study is derived from the 1-hour average product of the MERRA-2 tavg1_2d_aer_Nx dataset, and CO column concentration from the MERRA-2 tavg1_2d_chm_Nx. The spatial resolution of the two datasets is 0.625°×0.5°. During data processing, the 24-hour data of each day was averaged to obtain daily average data.

2.1.4 ERA5

ERA5 is a global atmospheric reanalysis dataset provided by the European Centre for Medium-range Weather Forecasting (ECMWF) (Zhao et al., 2020). In recent years, some studies have evaluated the accuracy of reanalysis data provided by ECMWF based on radiosonde data. For example, Luo et al. (2020) found that the average RH discrepancy between ERA-Interim radiosonde was within 10% below 500 hPa. Song et al. (2020) found that the root mean square error (RMSE) of ERA5 RH was 3.85% compared with the RH profile of the radiosonde. The above results show that RH from reanalysis data has good accuracy, and has been widely used in various research fields (Sajadi et al., 2020; Tzanis et al., 2019; Xiao et al., 2020). The RH data of ERA5 used in this paper is divided into 37 layers vertically (1 hPa–1000 hPa). The temporal resolution is 1 h and the spatial resolution is 0.125°×0.125°. In order to ensure the spatial consistency, the RH data (121.375° E, 31.25° N) closest to the location of Raman lidar was used.

2.2 Lidar data processing

Original signals need to be pre-processed before retrieval, including background subtraction, photon counting signal dead-time correction, gluing, and overlap correction (D'Amico et al., 2016). The calculation of the glue coefficients used the method proposed by Newsom et al. (2009). In order to reduce the influence of incompletely overlapping detection areas of lidar on retrieved results, only signals in the complete overlap area were used for retrieval. In addition, affected by the

location altitude of Raman lidar and the least square method used in the retrieval process, the lowest height of LR obtained by Raman method is 569.5m (ASL). Since Raman Lidar used in this study can detect the Raman scattering signal of 387nm nitrogen and signal-to-noise ratios of Raman signals in daytime are much lower than that in night time, the 355nm LR at night can be obtained through retrieval. The retrieval results of raw signals were counted by hour, and the hours with more than 15 minutes of retrieval results were regarded as effective observation hours. The retrieval results within the effective observation hours were averaged to obtain hourly average data. During observation period, data of 667 effective observation hours was obtained through retrieval and statistics. The monthly distribution is shown in Fig. 1.

There are many sources of errors in the retrieval results. The relative errors of particle extinction coefficients caused by assumed air density profile are 1.5% (Masonis, 2002), and the relative errors of particle backscatter coefficients caused by reference height can be 10% (Ansmann et al., 1992). The mean deviations of particle extinction coefficients caused by signal detection are within 15% in the 350 m–2000 m height range and within 20% in the 3000 m–4000 m height range (Pappalardo et al., 2004). The difference is caused by different signal-to-noise ratio at low altitude and high altitude. Due to the low signal-to-noise ratio, there are usually more missing values at high altitudes.

3 Results and discussions

3.1 LR temporal and vertical variations

3.1.1 General variation of LR

Figure. 2(a) shows the average profile of LR from 667 hours of statistical results. Because of variability of aerosol particle size and microphysical properties with height (Singh et al., 2005), the average LR were characterized by a large variability, ranging from 17 sr to 82 sr. LR reached the maximum at the height of 600m, and decreased with the increase of height. The average LR in the height range of 0.5 km–5 km was 41.0±22.5 sr, and relatively small of 24.8±13.7 sr above 2 km. These discrepancies were in good agreement to the results of Hee et al. (2016) in Malaysia with mostly less than 25 sr in the altitude range of 2 km to 3 km. LR depend on the aerosol size distribution and refractive index of aerosol particles (Takamura et al., 1994; Young et al., 1993). The small LR may be caused by shape effect of aerosol particles (not obviously nonspherical) and relatively low absorption efficiency (Tesche et al., 2007).

In order to investigate the variations of LR at different altitude ranges, Fig. 2(b) presents average LR at different altitude ranges. The average LR from 0.5 km to 1km was 68.2±19.5 sr, which was in good agreement with the 355nm LR observed by Ferrare et al. (2001) in Oklahom, America. The mean value of LR was between 40 sr and 50 sr in the altitude range of 1 km–2 km, and mean values of LR were usually less than 40 sr above 2km, which was related to low aerosol concentration and low absorption efficiency of aerosols (Hänel et al., 2012; Hee et al., 2016). Furthermore, the slope of LR for the different height ranges as shown in Fig. 2(b) also gradually decreased with the increased height. Below 3 km, LR decreased rapidly with the increase of altitude with the largest slope of -17.83 below 1.5 km. The reasons for this were that

temperature inversion in the low layer of the planetary boundary layer (PBL) at night weakened vertical movement of atmosphere and inhibited diffusion of pollutants emitted by human activities such as vehicles and fossil fuel combustion. The accumulation of pollutants in the low layer of the PBL resulted in significant differences of aerosol vertical distribution and a rapidly decreased aerosol extinction coefficient in the PBL (Liu et al., 2017; Wang et al., 2020). However, above 3km, the low aerosol concentration and homogeneous vertical distribution of aerosol led to small differences in LR at different height ranges.

Figure. 3 shows the frequency distribution of LR in different altitude range. Overall, LR were widely distributed in the altitude range of 0.5 km–5 km. In most cases (about 90%) LR ranged from 10 sr to 80 sr with the highest frequency of 17.3% between 40 sr and 50 sr. It should be noted that the number of observations trailed off at larger LR and the frequency of abnormally large LR (> 90 sr) was about 4%. LR also had a wide distribution range within 0.5 km–2 km, and the frequency of 40 sr–50 sr was the highest (24.6%), which was similar to the range of 0.5 km–5 km. Large LR (> 60 sr) were mainly distributed in the range of 0.5 km–2.0 km, suggesting that the aerosol in this height range had strongly absorbing ability. Although there were a few large LR (> 60 sr) above 2 km, LR was mainly distributed between 0 sr–40 sr with the highest frequency of 34% between 10 sr and 20 sr.

3.1.2 Temporal variations of LR

Figure. 4(a) presents seasonal variations of LR over Shanghai during observation period. The seasonal average LR was the largest with 47.6±25.1 sr in autumn and the lowest of 39.1±19.6sr in spring. Generally, the LR of aerosol particles with stronger absorption ability is larger (Müller et al., 2007). Black carbon (BC) has strong ability to absorb visible light (Chow et al., 2009), and aerosols rich in BC tend to show larger LR, such as biomass burning aerosols (Giannakaki et al., 2016). Shanghai area is easily affected by smoke produced by the burning of crop residues during the harvest season of autumn (Xu et al., 2018). According to the results of Wang et al. (2014), BC concentration in Shanghai was the lowest in spring and higher in autumn and winter. This indicated that aerosol absorbing ability in spring was weaker compared with that in autumn and winter.

Statistics of mean LR at different height range in each month were shown in Fig. 4(b). It can be addressed that LR of all months decreased with the increase of altitude. The average LR below 2 km was the largest in October, which was attributed to smoke aerosols produced by biomass burning in surrounding cities and rural areas during harvest season (Nie et al., 2015). In view of vertical variations of LR in different months, aerosols with LR > 40 sr were confined within 1.5 km from March to August, while the other months were 2 km, especially in October and November within 2.5 km. This revealed a point that the diffusion heights of aerosols with absorbing properties were characterized by a strong seasonality. In spring and summer, the diffusion height of absorbing aerosol was lower, on the contrary, it was higher in autumn and winter. The discrepancies in seasonal height distribution of aerosols can be attributed to the monsoon climate (He et al., 2006; Liu et al., 2020; Wang et al., 2016). Shanghai, on the southeast coast of China, was affected by the subtropical monsoon climate and the prevailing winds are southeast and northwest in spring and southeast in summer, respectively (Cai et al., 2010). Clean air from the sea

could reduce air pollution to a large extent by diluting the concentration of pollutants (Wang et al., 2014). In particular, the LR in March and April above 2.5 km were higher than those in other months, which may be due to the influence of dust aerosols brought by the prevailing northwest wind in spring. Liu et al. (2020) pointed out that dust aerosols from Inner Mongolia and Gobi desert had a high frequency in spring at an altitude of 3 km–5 km in Shanghai. The prevailing winds in autumn and winter were northeast and northwest, respectively. Absorbing aerosols originated from the north China resulted in relatively large LR at high altitude in Shanghai.

Liu et al. (2012) reported that vast majority aerosol particles in the Yangtze Delta region (including Shanghai) were below 2 km. In order to analyze the variation characteristics of LR in Shanghai more precisely, Fig. 5 shows LR of 667 effective observation hours below 2 km. The abnormally large LR (> 80 sr) were usually distributed in the PBL, meaning that local emissions were the main source of strongly absorbing aerosols. From this figure, one can also conclude that the number of larger LR within the PBL followed a decreasing trend with the passage of observation time, alluding to a gradually reduced emission of absorbing aerosols in Shanghai. This reduction was in good agreement with the reductions of BC and particulate matter (PM) concentrations caused by a series of energy-saving and emission-reduction measures such as the Shanghai Clean Air Action Plan (2018–2022) implemented by the Shanghai government in recent years (Wei et al., 2020).

3.2 Analysis of influencing factors of LR

3.2.1 Reasons for LR variations with height

From Eq. (1), we find that LR are negatively correlated with $P(\pi)$, and the nonspherical geometry of particles can cause a reduction of the $P(\pi)$ (Müller, 2003). δ can reflect the regularity of particle shape (Novitsky and Philbrick, 2005), and are usually defined as the ratios of vertical backscatter coefficients and parallel backscatter coefficients (Behrendt and Nakamura, 2002). The smaller the value of δ, the more regular the shape of particles, i.e., the closer the particle shape is to the spherical (Gobbi, 1998). Since the Raman depolarization lidar used in this study can only detect the polarization information of 532 nm channel, δ at 532 nm were used to analyze the sphericity of particles. It can be seen from Fig. 6(a) that LR were proportional to δ with a correlation coefficient of 0.86, which was consistent with Reagan's (1988) study that LR increased with the increase of particle asphericity. LR is the ratio of the extinction coefficient and the backscatter coefficient. Generally, there are two reasons for the increase of LR with the increasing particle asphericity. On the one hand, the backscatter coefficient decreases significantly with the increase of particle asphericity, on the other hand, the extinction coefficient is sensitive to the cross-section of the particle and is less affected by the shape of particles.

It is worth noting that LR which responses to large depolarization ratio are in range of 100 sr–120 sr. Generally, the LR of dust aerosol with large depolarization ratio was between 40 sr and 60 sr (Murayama et al., 2004; Noh et al., 2007). Hee et al. (2016) found that 355nm LR of aged forest fire aerosols was relatively large, ranging from 80sr to120sr. And previous studies have found that some aged forest fire aerosols also show large depolarization ratios (Hu et al., 2019; Murayama et al.,

2004). There might be two reasons for this phenomenon. One is that dust aerosols on the surface are lifted into the biomass burning plume (Müller et al., 2007), and the other is nonsphericity of particles due to coagulation of smoke particles during aging process (Reid et al., 1998). Therefore, the LR in the range of 100 sr–120 sr corresponds to large DR may be caused by aged forest fire aerosols. In order to explore whether the decrease of LR with increasing height is affected by the particle shape effect, Fig. 6(b) shows the average profile of δ at lidar observation time. The average and median of δ gradually decreased with the increase of height, indicating that the shape of particles became more regular with the increase of height. This result evidenced the inferences of Tesche et al. (2007) that the regular particle shape was one of the reasons for the smaller LR at high altitudes.

3.2.2 Influences of aerosol sources on LR

In order to further research the influences of wind directions on LR and its vertical distribution, cluster analysis of back trajectories was used to study the transport of atmospheric aerosols. Based on the HYSPLIT-4 model (Franke et al., 2001; Noh et al., 2007), the 72-hour backward trajectories at the height of 1000m were shown in Fig. 7(a). The cluster analysis resulted in 4 main air mass directions (Hänel et al., 2012; Pietruczuk and Podgorski, 2009). Backward trajectory cluster analysis based on HYSPLIT model is widely used in atmospheric aerosol research (Wang et al., 2020; Xu et al., 2018; Zhang et al., 2020). We performed a significance test on the results of the cluster analysis, and the one-way ANOVA showed that $P<0.05$, indicating that the LR of the four clusters were significantly different. Similarly, there were significant differences in δ among the four clusters.

The mean LR and δ between 0.5 km and 5 km of the four clusters are shown in Fig. 2(b), and Fig. 7(c) presents the distribution of LR and δ at different heights of four clusters. The mean LR (38.7±24.2 sr) and δ (0.030±0.021) of air mass 1 were the lowest in all clusters. As air mass 1 came from the Western Pacific Ocean, it could bring abundant marine aerosols. Sea salt particles are characterized by coarse mode, which are spherical in wet conditions. In addition, marine aerosols have lower LR than dust aerosols because of their weak absorption ability (Papagiannopoulos et al., 2018). Interestingly, the LR at 355nm of clean marine aerosols were usually between 20 sr and 35 sr (Alexander and Protat, 2019; Hee et al., 2016), which is smaller than that of aerosols brought by air mass 1 in the study. It was observed that the average LR in the range of 0.5 km–1 km was more than 60 sr, which suggested that the clean marine aerosols from the sea might be mixed with local absorptive aerosols in Shanghai (Franke et al., 2001; Müller et al., 2007).

The average LR affected by the aerosols brought by air mass 2 was approximately equivalent to the LR affected by air mass 1, with an average value of 39.4±19 sr at 0.5 km–5 km altitude. The source region of air mass 2 was located in the Inner Mongolia, which could bring dust aerosols. During the transport over the ocean, clean marine aerosols mixed with dust aerosols led to the LR larger than that of the clean marine aerosols.

The mean LR of air mass 3 was 44.2±24.7 sr, largest in the four clusters. As the air mass 3 passed through the northern China region where pollution level and pollution amount were relatively high, the aerosol particles brought by the air mass had strongly absorbing ability. In addition, it was evident that δ corresponding to air mass 3 below 2.5 km were larger than

that of the other three air masses in Fig. 7(c). The larger δ hinted at a high contribution of irregularly shaped aerosol particles. Air mass 3 passing through dust source areas of Mongolia and Inner Mongolia could bring abundant dust aerosols to the Shanghai (Huang et al., 2012). Dust aerosols usually show larger particle depolarization ratios than other types of aerosols due to the irregular particle shape (Kai et al., 2008; Murayama et al., 1999). For example, Huang et al. (2012) found that aerosol depolarization ratios at 532 nm in the case of dust pollution were significantly greater than that in the cases of secondary inorganic pollution and biomass burning pollution. As a consequence, the larger δ corresponding to air mass 3 were attributed to dust aerosols, and long-range transported dust aerosols could reach a height of about 2.5 km.

The average LR affected by aerosols from air mass 4 was 42.6±21.8 sr. It should be noted that the average δ affected by aerosols brought by air mass 4 was small, which was comparable to that of air mass 1, indicating a high contribution of spherical aerosol particles, but LR was larger. By observing the trajectory of air mass 4, we found that it passed through Hubei Province with high industrial level (Wang et al., 2016) and Anhui Province with heavy pollution of biomass burning (Wu et al., 2020). The accompanying industrial and smoke aerosols, which are approximately spherical (Giannakaki et al., 2016; Müller et al., 2007) could be responsible for the smaller δ.

In summary, the variations and vertical distribution of LR and δ in Shanghai were caused by the synthetic impacts of long-range transport from different source areas and local emissions. The larger LR and δ are the results of smoke and dust aerosols from the northwest, and the mixing of aerosols accompanied by air masses from the sea and locally emitted absorbing aerosols resulted in smaller δ and slightly larger LR than that of clean marine aerosols.

3.2.3 Influence of atmospheric turbidity on LR

AOD is an important parameter to characterize optical properties of aerosols, which can reflect the content of aerosols in the atmosphere, and also is an important index to evaluate atmospheric quality and visibility (Cheng et al., 2015; Hess et al., 1998). Previous studies have shown a positive correlation between AOD and LR by analyzing the average LR in different AOD ranges (Ferrare et al., 2001; He et al., 2006), due to the increase of aerosol absorption and extinction caused by the increase of small particles (Takamura et al., 1994). In addition, although some studies have analyzed the vertical profiles of LR in different pollution degree cases, the main concern was average LR of aerosol layer (Chen et al., 2014; Wang et al., 2016). As mentioned previously, the vertical variations of absorbing aerosols and their influencing factors played an important role in evaluating the radiation effect of aerosol and studying the cause of pollution (Mishchenko et al., 2004). Consequently, it is meaningful to study the vertical variations of LR under different atmospheric turbidity.

AOD was obtained by integrating 355nm extinction coefficients in the range of 0.5 km–2 km. The average profile of LR below 2 km in different AOD ranges was drawn as shown in Fig. 8. Under clean condition, LR decreased more dramatically with the increase of height. By contrast, the lack of significant vertical variability of LR in the case of high atmospheric turbidity illustrate the homogenous vertical distribution of absorbing aerosols. The result that vertical slope of LR presented a decreasing trend with the increasing atmospheric turbidity can be explained by aerosol radiative effects on

thermal structure and atmospheric stability. In the case of high atmospheric turbidity, aerosol particles that absorb a large amount of solar radiation during the day radiatively warm the surface at night, but radiatively cool the air above the surface (Jacobson and Kaufman, 2006; Ramanathan et al., 2005). The decrease in the atmosphere stability due to temperature difference increase vertical turbulence and results in the homogeneous vertical distribution of aerosols. On the contrary, in the clear and pollution-free nights, the surface radiation cooling results in temperature inversions near the ground. The stable atmosphere is not conducive to the lifting of absorbing aerosols, resulting in a large vertical variation of LR.

3.3 The main aerosol types causing the abnormal variation of LR

As shown in Fig. 5, abnormally large LR occurred occasionally in relative high location approximately above the top of PBL in spite of an usually decay trend of LR with height. To investigate the reason, we selected five days with LR > 80 sr over 1 km. According to previous reports, biomass burning aerosols are relatively small and spherical, and their strong absorption ability makes them have large LR (Papagiannopoulos et al., 2018). For example, Amiridis et al. (2009) observed smoke plume from biomass burning over Greece and found that 355nm LR ranged from 40sr to 100sr. Giannakaki et al. (2016) used Raman lidar in South Africa and found that 355nm LR of biomass burning aerosols was 92±10 sr. Generally, the determination of aerosol type with large LR observed by Raman lidar was based on fire data and backward trajectory model such as HYSPLIT (Hee et al., 2016; Noh et al., 2008). In our study, spatial distribution of biomass burning tracers were used to determine whether the abnormally large LR was related to biomass burning aerosols (Huang et al., 2012), which could lay a foundation for future research on aerosol three-dimensional spatial distribution and pollution causes.

Biomass burning is one of the important sources of PM, organic carbon (OC) and black carbon (BC) in the atmosphere (Wu et al., 2020). It also emits pollutant gases such as CO, SO2, NOx and HCN (Andreae and Merlet, 2001; Kalluri et al., 2020; Randel et al., 2010). CO can be used as a tracer for biomass burning. For example, Huang et al. (2012) found that CO column concentration in the biomass burning zone was significantly different from that in the non-biomass burning zone. In addition, it would also result in high AOD and AAOD (absorbing aerosol optical depth) in the region due to strong absorption of biomass burning aerosols (Shaik et al., 2019). For example, He et al. (2015) found that AOD at 500nm increased from 0.73 to 1.00 when analyzing the smoke plume of biomass burning in Shanghai. Similarly, Vadrevu et al. (2011) found that AOD of wheat dregs burning season and rice dregs burning season were both high by using satellite data in India, which were 0.598 and 0.58, respectively. CAOD is the optical depth of carbon aerosol, which is the sum of the optical depth of black carbon and organic carbon aerosol. Hence, AOD, AAOD, CAOD at 550nm, and CO column concentrations were used as tracers to determine whether these five cases were affected by biomass burning. Figure. 9 depicts the spatial distribution of four tracers in five cases. AOD in Shanghai during these five days ranged from 0.45 to 1.05, pointing to heavy aerosol pollution. The average value of AAOD was between 0.0375 and 0.1, and CAOD was between 0.12 and 0.24, which reasonably demonstrate the presence of absorbing aerosols and carbon aerosols in Shanghai (Shaik et al., 2019). In addition, the CO column concentrations in Shanghai for these five days were relatively high, all more than 9×10^{-4}

kg/m^2, which illustrate significant possibility of smoke advection. Therefore, it could be inferred that Shanghai was affected by biomass burning aerosols from local rural areas or neighboring provinces in the five cases.

Even if the abnormally large LR above 1km was mainly relevant for the advection of biomass burning aerosols, it should be noted that the increasing aerosol extinction caused by increase of RH could also result in large LR (Salemink et al., 1984). For example, Ackerman (1998) found that LR of continental aerosols increased from 40 sr to 80 sr with RH. Figure. 10 presents LR and RH profiles at three times. Above 1km, LR was a function of RH, and abnormally large LR had a good corresponding relationship with high RH, which demonstrated that the abnormally larger LR above 1km was also related to high RH.

4 Conclusions

For the first time, long-term (2017–2019) observation of Raman lidar was carried out in Shanghai. The aerosol LR at 355nm were retrieved, and the variations of LR and their influencing factors were analyzed in detail based on 667-hour data. In the height range of 0.5 km–5 km, about 90% of LR were distributed in 10 sr–80 sr, with an average of 41.0±22.5 sr, and LR decreased with the increase of height. The average LR in autumn was the largest, which was 47.6±25.1 sr. The LR in summer and winter were close, 41.0±21.6 sr and 42.0±27.3 sr, respectively, and the LR in spring was the smallest. The seasonal variation of LR was closely related to the seasonal variations of BC concentration. In the height range of 0.5 km–2 km, the average LR was the largest in October, which was relevant for the biomass burning aerosols produced by burning straw in the surrounding cities and rural areas during the harvest season. In addition, affected by the prevailing winds in spring and summer, the aerosols with LR > 40sr were confined within 1.5 km from March to August.

LR and δ were positively correlated, meaning that the more regular the particle shape, the smaller the LR. δ decreased with the increase of height, which proved that the particle shape was one of the factors affecting the vertical distribution of LR. LR had a strong dependence on the source directions of air masses. Large LR coincided with the air masses from the northwest, while the air masses from the east led to small LR. In addition, the shape of aerosol particles was the most irregular due to aerosols brought by air masses from the northwest. The vertical distribution of LR was affected by atmospheric turbidity, the smaller the AOD, the greater the vertical change of LR.

For the abnormal change which was different from an decay trend of LR with height, we analyzed the spatial distribution of 500 nm AOD, AAOD, CAOD and CO column concentrations of five cases with LR >80 sr over 1km, and found that Shanghai was located in or affected by high value centers. Therefore, it could be inferred that large LR above 1km in Shanghai were relevant for biomass burning aerosols. In addition, the large LR above 1km at some times was also related to high RH.

Data availability

The data presented in this paper are available from the corresponding authors upon request.

Competing interests

The authors declare that they have no conflict of interest.

Author contributions

TL retrieved the data and wrote the paper. QH and YC formulated the project goals and edited and reviewed the manuscript. JL, QL and WG downloaded and analyzed the reanalysis data. GH, WS and XY revised the manuscript.

Acknowledgments

We are grateful to the NASA for providing MERRA-2 data and the NOAA Air Resources Laboratory (ARL) for the provision of the HYSPLIT transport and dispersion model. And, we also gratefully acknowledge the ECMWF for the provision of the ERA5 dataset.

Financial support

This work was supported by the National Key R&D Program of China (Grant No. 2016YFC0201900); the National Natural Science Foundation of China (Grant No. 41975029); the Science Research Project of Shanghai Meteorological Service (Grant No. MS202016); the Chinese Ministry of Science and Technology (Grant No. 2018YFC1506305); the National Natural Science Foundation of China (Grant No. 91644211), and the Fundamental Research Funds for the Central Universities (Grant No. 2232019D3-27).

References

Ackermann, J., 1998. The extinction-to-backscatter ratio of tropospheric aerosol: A numerical study. J Atmos Ocean Tech 15, 1043-1050.

Alexander, S.P., Protat, A., 2019. Vertical Profiling of Aerosols With a Combined Raman‐Elastic Backscatter Lidar in the Remote Southern Ocean Marine Boundary Layer (43–66°S, 132–150°E). J Geophys Res-Atmos 124, 12107-12125.

Amiridis, V., Balis, D.S., Giannakaki, E., Stohl, A., Kazadzis, S., Koukouli, M.E., Zanis, P., 2009. Optical characteristics of biomass burning aerosols over Southeastern Europe determined from UV-Raman lidar measurements. Atmos Chem

Phys 9, 2431-2440.

Andreae, M.O., Merlet, P., 2001. Emission of trace gases and aerosols from biomass burning. Global Biogeochemical Cycles 15, 955-966.

Ansmann, A., Riebesell, M., Wandinger, U., Weitkamp, C., Voss, E., Lahmann, W., Michaelis, W., 1992. Combined Raman Elastic-Backscatter Lidar for Vertical Profiling of Moisture, Aerosol Extinction, Backscatter, and Lidar Ratio. Applied Physics B-Photophysics and Laser Chemistry 55, 18-28.

Behrendt, A., Nakamura, T., 2002. Calculation of the calibration constant of polarization lidar and its dependency on atmospheric temperature. Opt Express 10, 805-817.

Cai, C., Geng, F., Tie, X., Yu, Q., An, J., 2010. Characteristics and source apportionment of VOCs measured in Shanghai, China. Atmospheric Environment 44, 5005-5014.

Chen, Z., Liu, W., Heese, B., Althausen, D., Baars, H., Cheng, T., Shu, X., Zhang, T., 2014. Aerosol optical properties observed by combined Raman-elastic backscatter lidar in winter 2009 in Pearl River Delta, south China. J Geophys Res-Atmos 119, 2496-2510.

Cheng, T., Xu, C., Duan, J., Wang, Y., Leng, C., Tao, J., Che, H., He, Q., Wu, Y., Zhang, R., Li, X., Chen, J., Kong, L., Yu, X., 2015. Seasonal variation and difference of aerosol optical properties in columnar and surface atmospheres over Shanghai. Atmospheric Environment 123, 315-326.

Chow, J.C., Watson, J.G., Doraiswamy, P., Chen, L.-W.A., Sodeman, D.A., Lowenthal, D.H., Park, K., Arnott, W.P., Motallebi, N., 2009. Aerosol light absorption, black carbon, and elemental carbon at the Fresno Supersite, California. Atmospheric Research 93, 874-887.

D'Amico, G., Amodeo, A., Mattis, I., Freudenthaler, V., Pappalardo, G., 2016. EARLINET Single Calculus Chain – technical – Part 1: Pre-processing of raw lidar data. Atmospheric Measurement Techniques 9, 491-507.

Fan, S., Liu, C., Xie, Z., Dong, Y., Hu, Q., Fan, G., Chen, Z., Zhang, T., Duan, J., Zhang, P., Liu, J., 2018. Scanning vertical distributions of typical aerosols along the Yangtze River using elastic lidar. Sci Total Environ 628-629, 631-641.

Fernald, F.G., 1984. Analysis of atmospheric lidar observations: some comments. Optical Society of America.

Ferrare, R.A., Turner, D.D., Brasseur, L.H., Feltz, W.F., Dubovik, O., Tooman, T.P., 2001. Raman lidar measurements of the aerosol extinction-to-backscatter ratio over the Southern Great Plains. J Geophys Res-Atmos 106, 20333-20347.

Franke, K., Ansmann, A., Muller, D., Althausen, D., Wagner, A., Scheele, R., 2001. One-year observations of particle lidar ratio over the tropical Indian Ocean with Raman lidar. Geophysical Research Letters 28, 4559-4562.

Gelaro, R., McCarty, W., Suarez, M.J., Todling, R., Molod, A., Takacs, L., Randles, C., Darmenov, A., Bosilovich, M.G., Reichle, R., Wargan, K., Coy, L., Cullather, R., Draper, C., Akella, S., Buchard, V., Conaty, A., da Silva, A., Gu, W., Kim, G.K., Koster, R., Lucchesi, R., Merkova, D., Nielsen, J.E., Partyka, G., Pawson, S., Putman, W., Rienecker, M., Schubert, S.D., Sienkiewicz, M., Zhao, B., 2017. The Modern-Era Retrospective Analysis for Research and Applications, Version 2 (MERRA-2). J Clim Volume 30, 5419-5454.

Giannakaki, E., van Zyl, P.G., Müller, D., Balis, D., Komppula, M., 2016. Optical and microphysical characterization of

aerosol layers over South Africa by means of multi-wavelength depolarization and Raman lidar measurements. Atmos Chem Phys 16, 8109-8123.

Gobbi, G.P., 1998. Polarization lidar returns from aerosols and thin clouds: a framework for the analysis. Appl Opt 37, 5505-5508.

Gong, W., Liu, B., Ma, Y., Zhang, M., 2015. Mie LIDAR Observations of Tropospheric Aerosol over Wuhan. Atmosphere 6, 1129-1140.

Hänel, A., Baars, H., Althausen, D., Ansmann, A., Engelmann, R., Sun, J.Y., 2012. One-year aerosol profiling with EUCAARI Raman lidar at Shangdianzi GAW station: Beijing plume and seasonal variations. Journal of Geophysical Research: Atmospheres 117, n/a-n/a.

He, Q., Zhao, X., Lu, J., Zhou, G., Yang, H., Gao, W., Yu, W., Cheng, T., 2015. Impacts of biomass-burning on aerosol properties of a severe haze event over Shanghai. Particuology 20, 52-60.

He, Q.S., Li, C.C., Mao, J.T., Lau, A.K.H., Li, P.R., 2006. A study on the aerosol extinction-to-backscatter ratio with combination of micro-pulse LIDAR and MODIS over Hong Kong. Atmos Chem Phys 6, 3243-3256.

Hee, W.S., Lim, H.S., Jafri, M.Z.M., Lolli, S., Ying, K.W., 2016. Vertical Profiling of Aerosol Types Observed across Monsoon Seasons with a Raman Lidar in Penang Island, Malaysia. Aerosol and Air Quality Research 16, 2843-2854.

Hess, M., Koepke, P., Schult, I., 1998. Optical properties of aerosols and clouds: The software package OPAC. B Am Meteorol Soc 79, 831-844.

Hu, Q., Goloub, P., Veselovskii, I., Bravo-Aranda, J.-A., Popovici, I.E., Podvin, T., Haeffelin, M., Lopatin, A., Dubovik, O., Pietras, C., Huang, X., Torres, B., Chen, C., 2019. Long-range-transported Canadian smoke plumes in the lower stratosphere over northern France. Atmos Chem Phys 19, 1173-1193.

Huang, K., Zhuang, G., Lin, Y., Fu, J.S., Wang, Q., Liu, T., Zhang, R., Jiang, Y., Deng, C., Fu, Q., Hsu, N.C., Cao, B., 2012. Typical types and formation mechanisms of haze in an Eastern Asia megacity, Shanghai. Atmos Chem Phys 12, 105-124.

Jacobson, M.Z., 1998. Studying the effects of aerosols on vertical photolysis rate coefficient and temperature profiles over an urban airshed. Journal of Geophysical Research: Atmospheres 103, 10593-10604.

Jacobson, M.Z., Kaufman, Y.J., 2006. Wind reduction by aerosol particles. Geophysical Research Letters 33.

Kai, K., Nagata, Y., Tsunematsu, N., Matsumura, T., Kim, H.-S., Matsumoto, T., Hu, S., Zhou, H., Abo, M., Nagai, T., 2008. The Structure of the Dust Layer over the Taklimakan Deser during the Dust Storm in April 2002 as Observed Using a Depolarization Lidar. J Meteorol Soc Jpn 86, 1-16.

Kalluri, R.O.R., Zhang, X., Bi, L., Zhao, J., Yu, L., Kotalo, R.G., 2020. Carbonaceous aerosol emission reduction over Shandong province and the impact of air pollution control as observed from synthetic satellite data. Atmospheric Environment 222.

Kim, M.H., Omar, A.H., Tackett, J.L., Vaughan, M.A., Winker, D.M., Trepte, C.R., Hu, Y., Liu, Z., Poole, L.R., Pitts, M.C., Kar, J., Magill, B.E., 2018. The CALIPSO Version 4 Automated Aerosol Classification and Lidar Ratio Selection

Algorithm. Atmos Meas Tech 11, 6107-6135.

Koren, I., Kaufman, Y.J., Remer, L.A., Martins, J.V., 2004. Measurement of the effect of Amazon smoke on inhibition of cloud formation. Science 303, 1342-1345.

Liu, D., Kanitz, T., Ciapponi, A., Mondello, A., D'Ottavi, A., Mateo, A.B., Straume, A.-G., Voland, C., Bon, D., Checa, E., Alvarez, E., Bellucci, I., Do Carmo, J.P., Brewster, J., Marshall, J., Schillinger, M., Hannington, M., Rennie, M., Reitebuch, O., Lecrenier, O., Bravetti, P., Sacchieri, V., De Sanctis, V., Lefebvre, A., Parrinello, T., Wernham, D., Wang, Y., Wu, Y., Gross, B., Moshary, F., 2020. ESA's Lidar Missions Aeolus and EarthCARE. EPJ Web of Conferences 237.

Liu, J., Zheng, Y., Li, Z., Flynn, C., Cribb, M., 2012. Seasonal variations of aerosol optical properties, vertical distribution and associated radiative effects in the Yangtze Delta region of China. Journal of Geophysical Research: Atmospheres 117, n/a-n/a.

Liu, Q., He, Q., Fang, S., Guang, Y., Ma, C., Chen, Y., Kang, Y., Pan, H., Zhang, H., Yao, Y., 2017. Vertical distribution of ambient aerosol extinctive properties during haze and haze-free periods based on the Micro-Pulse Lidar observation in Shanghai. Sci Total Environ 574, 1502-1511.

Liu, Q., Liu, X., Liu, T., Kang, Y., Chen, Y., Li, J., Zhang, H., 2020. Seasonal variation in particle contribution and aerosol types in Shanghai based on satellite data from MODIS and CALIOP. Particuology 51, 18-25.

Lv, L., Xiang, Y., Zhang, T., Chai, W., Liu, W., 2020. Comprehensive study of regional haze in the North China Plain with synergistic measurement from multiple mobile vehicle-based lidars and a lidar network. Sci Total Environ 721, 137773.

Ma, X., Wang, C., Han, G., Ma, Y., Li, S., Gong, W., Chen, J., 2019. Regional Atmospheric Aerosol Pollution Detection Based on LiDAR Remote Sensing. Remote Sensing 11.

Masonis, S.J., 2002. An intercomparison of aerosol light extinction and 180° backscatter as derived using in situ instruments and Raman lidar during the INDOEX field campaign. Journal of Geophysical Research 107.

McComiskey, A., Schwartz, S.E., Schmid, B., Guan, H., Lewis, E.R., Ricchiazzi, P., Ogren, J.A., 2008. Direct aerosol forcing: Calculation from observables and sensitivities to inputs. Journal of Geophysical Research 113.

Mehta, M., Singh, N., Anshumali, 2018. Global trends of columnar and vertically distributed properties of aerosols with emphasis on dust, polluted dust and smoke - inferences from 10-year long CALIOP observations. Remote Sensing of Environment 208, 120-132.

Mishchenko, M.I., Cairns, B., Hansen, J.E., Travis, L.D., Burg, R., Kaufman, Y.J., Vanderlei Martins, J., Shettle, E.P., 2004. Monitoring of aerosol forcing of climate from space: analysis of measurement requirements. Journal of Quantitative Spectroscopy and Radiative Transfer 88, 149-161.

Müller, D., 2003. Saharan dust over a central European EARLINET-AERONET site: Combined observations with Raman lidar and Sun photometer. Journal of Geophysical Research 108.

Müller, D., Ansmann, A., Mattis, I., Tesche, M., Wandinger, U., Althausen, D., Pisani, G., 2007. Aerosol-type-dependent lidar ratios observed with Raman lidar. Journal of Geophysical Research 112.

Murayama, T., Müller, D., Wada, K., Shimizu, A., Sekiguchi, M., Tsukamoto, T., 2004. Characterization of Asian dust and

Siberian smoke with multi-wavelength Raman lidar over Tokyo, Japan in spring 2003. Geophysical Research Letters 31.

Murayama, T., Okamoto, H., Kaneyasu, N., Kamataki, H., Miura, K., 1999. Application of lidar depolarization measurement in the atmospheric boundary layer: Effects of dust and sea-salt particles. Journal of Geophysical Research: Atmospheres 104, 31781-31792.

Newsom, R.K., Turner, D.D., Mielke, B., Clayton, M., Ferrare, R., Sivaraman, C., 2009. Simultaneous analog and photon counting detection for Raman lidar. Appl Opt 48, 3903-3914.

Nicolae, D., Donovan, D., Zadelhoff, G.-J.v., Daou, D., Wandinger, U., Makoto, A., Vassilis, A., Balis, D., Behrendt, A., Comeron, A., Gibert, F., Landulfo, E., McCormick, M.P., Senff, C., Veselovskii, I., Wandinger, U., 2018. Earthcare atlid extinction and backscatter retrieval algorithms. EPJ Web of Conferences 176.

Nie, W., Ding, A.J., Xie, Y.N., Xu, Z., Mao, H., Kerminen, V.M., Zheng, L.F., Qi, X.M., Huang, X., Yang, X.Q., Sun, J.N., Herrmann, E., Petäjä, T., Kulmala, M., Fu, C.B., 2015. Influence of biomass burning plumes on HONO chemistry in eastern China. Atmos Chem Phys 15, 1147-1159.

Noh, Y.M., Kim, Y.J., Choi, B.C., Murayama, T., 2007. Aerosol lidar ratio characteristics measured by a multi-wavelength Raman lidar system at Anmyeon Island, Korea. Atmospheric Research 86, 76-87.

Noh, Y.M., Kim, Y.J., Müller, D., 2008. Seasonal characteristics of lidar ratios measured with a Raman lidar at Gwangju, Korea in spring and autumn. Atmospheric Environment 42, 2208-2224.

Novitsky, E.J., Philbrick, C.R., 2005. Multistatic lidar profiling of urban atmospheric aerosols. J Geophys Res-Atmos 110.

Omar, A.H., Winker, D.M., Vaughan, M.A., Hu, Y., Trepte, C.R., Ferrare, R.A., Lee, K.-P., Hostetler, C.A., Kittaka, C., Rogers, R.R., Kuehn, R.E., Liu, Z., 2009. The CALIPSO Automated Aerosol Classification and Lidar Ratio Selection Algorithm. J Atmos Ocean Tech 26, 1994-2014.

Painemal, D., Clayton, M., Ferrare, R., Burton, S., Josset, D., Vaughan, M., 2019. Novel aerosol extinction coefficients and lidar ratios over the ocean from CALIPSO–CloudSat: evaluation and global statistics. Atmospheric Measurement Techniques 12, 2201-2217.

Papagiannopoulos, N., Mona, L., Amodeo, A., amp, apos, Amico, G., Gumà Claramunt, P., Pappalardo, G., Alados-Arboledas, L., Guerrero-Rascado, J.L., Amiridis, V., Kokkalis, P., Apituley, A., Baars, H., Schwarz, A., Wandinger, U., Binietoglou, I., Nicolae, D., Bortoli, D., Comerón, A., Rodríguez-Gómez, A., Sicard, M., Papayannis, A., Wiegner, M., 2018. An automatic observation-based aerosol typing method for EARLINET. Atmos Chem Phys 18, 15879-15901.

Pappalardo, G., Amodeo, A., Pandolfi, M., Wandinger, U., Ansmann, A., Bosenberg, J., Matthias, V., Amiridis, V., De Tomasi, F., Frioud, M., Larlori, M., Komguem, L., Papayannis, A., Rocadenbosch, F., Wang, X., 2004. Aerosol lidar intercomparison in the framework of the EARLINET project. 3. Raman lidar algorithm for aerosol extinction, backscatter, and lidar ratio. Appl Opt 43, 5370-5385.

Pietruczuk, A., Podgorski, J., 2009. The lidar ratio derived from sun-photometer measurements at Belsk Geophysical Observatory. Acta Geophysica 57, 476-493.

Ramanathan, V., Chung, C., Kim, D., Bettge, T., Buja, L., Kiehl, J.T., Washington, W.M., Fu, Q., Sikka, D.R., Wild, M., 2005. Atmospheric brown clouds: impacts on South Asian climate and hydrological cycle. Proc Natl Acad Sci U S A 102, 5326-5333.

Randel, W.J., Park, M., Emmons, L., Kinnison, D., Bernath, P., Walker, K.A., Boone, C., Pumphrey, H., 2010. Asian monsoon transport of pollution to the stratosphere. Science 328, 611-613.

Reagan, J.A., Apte, M.V., Ben-David, A., Herman, B.M., 1988. Assessment of Aerosol Extinction to Backscatter Ratio Measurements Made at 694.3 Nm in Tucson, Arizona. Aerosol Science and Technology 8, 215-226.

Reid, J.S., Hobbs, P.V., Ferek, R.J., Blake, D.R., Martins, J.V., Dunlap, M.R., Liousse, C., 1998. Physical, chemical, and optical properties of regional hazes dominated by smoke in Brazil. Journal of Geophysical Research: Atmospheres 103, 32059-32080.

Salemink, H.W.M., Schotanus, P., Bergwerff, J.B., 1984. Quantitative Lidar at 532 nm for Vertical Extinction Profiles and the Effect of Relative Humidity Applied Physics B.

Shaik, D.S., Kant, Y., Mitra, D., Singh, A., Chandola, H.C., Sateesh, M., Babu, S.S., Chauhan, P., 2019. Impact of biomass burning on regional aerosol optical properties: A case study over northern India. J Environ Manage 244, 328-343.

Sicard, M., Rocadenbosch, F., Reba, M.N.M., Comerón, A., Tomás, S., García-Vízcaino, D., Batet, O., Barrios, R., Kumar, D., Baldasano, J.M., 2011. Seasonal variability of aerosol optical properties observed by means of a Raman lidar at an EARLINET site over Northeastern Spain. Atmos Chem Phys 11, 175-190.

Singh, U.N., Pappalardo, G., Mizutani, K., Amodeo, A., Mona, L., Pandolfi, M., 2005. Systematic measurements of the aerosol extinction-to-backscatter ratio, Lidar Remote Sensing for Industry and Environmental Monitoring V.

Takamura, T., Sasano, Y., Hayasaka, T., 1994. Tropospheric aerosol optical properties derived from lidar, sun photometer, and optical particle counter measurements. Appl Opt 33, 7132-7140.

Tesche, M., Ansmann, A., Muller, D., Althausen, D., Engelmann, R., Hu, M., Zhang, Y., 2007. Particle backscatter, extinction, and lidar ratio profiling with Raman lidar in south and north China. Appl Opt 46, 6302-6308.

Twomey, 1977. The Influence of Pollution on the Shortwave Albedo of Clouds. Journal of the Atmospheric Sciences 34, 1149-1152.

Vadrevu, K.P., Ellicott, E., Badarinath, K.V., Vermote, E., 2011. MODIS derived fire characteristics and aerosol optical depth variations during the agricultural residue burning season, north India. Environ Pollut 159, 1560-1569.

Walker, M., Venable, D., Whiteman, D.N., 2014. Gluing for Raman lidar systems using the lamp mapping technique. Appl Opt 53, 8535-8543.

Wandinger, U., Freudenthaler, V., Baars, H., Amodeo, A., Engelmann, R., Mattis, I., Groß, S., Pappalardo, G., Giunta, A., amp, apos, Amico, G., Chaikovsky, A., Osipenko, F., Slesar, A., Nicolae, D., Belegante, L., Talianu, C., Serikov, I., Linné, H., Jansen, F., Apituley, A., Wilson, K.M., de Graaf, M., Trickl, T., Giehl, H., Adam, M., Comerón, A., Muñoz-Porcar, C., Rocadenbosch, F., Sicard, M., Tomás, S., Lange, D., Kumar, D., Pujadas, M., Molero, F., Fernández, A.J., Alados-Arboledas, L., Bravo-Aranda, J.A., Navas-Guzmán, F., Guerrero-Rascado, J.L., Granados-Muñoz, M.J.,

Preißler, J., Wagner, F., Gausa, M., Grigorov, I., Stoyanov, D., Iarlori, M., Rizi, V., Spinelli, N., Boselli, A., Wang, X., Lo Feudo, T., Perrone, M.R., De Tomasi, F., Burlizzi, P., 2016. EARLINET instrument intercomparison campaigns: overview on strategy and results. Atmospheric Measurement Techniques 9, 1001-1023.

Wang, H., He, Q., Chen, Y., Kang, Y., 2014. Characterization of black carbon concentrations of haze with different intensities in Shanghai by a three-year field measurement. Atmospheric Environment 99, 536-545.

Wang, L., Lyu, B., Bai, Y., 2020. Aerosol vertical profile variations with seasons, air mass movements and local PM2.5 levels in three large China cities. Atmospheric Environment 224.

Wang, P., Che, H., Zhang, X., Song, Q., Wang, Y., Zhang, Z., Dai, X., Yu, D., 2010. Aerosol optical properties of regional background atmosphere in Northeast China. Atmospheric Environment 44, 4404-4412.

Wang, T., Han, Y., Huang, J., Sun, M., Jian, B., Huang, Z., Yan, H., 2020. Climatology of dust-forced radiative heating over the Tibetan Plateau and its surroundings, J Geophys Res-Atmos 125.

Wang, W., Gong, W., Mao, F., Pan, Z., Liu, B., 2016. Measurement and Study of Lidar Ratio by Using a Raman Lidar in Central China. Int J Environ Res Public Health 13.

Wei, C., Wang, M.H., Fu, Q.Y., Dai, C., Huang, R., Bao, Q., 2020. Temporal Characteristics and Potential Sources of Black Carbon in Megacity Shanghai, China. Journal of Geophysical Research: Atmospheres 125.

Welton, E.J., Campbell, J.R., Spinhirne, J.D., Scott, V.S., 2001. Global monitoring of clouds and aerosols using a network of micro-pulse lidar systems. Proc Spie 4153, 151-158.

Wu, J., Kong, S., Wu, F., Cheng, Y., Zheng, S., Qin, S., Liu, X., Yan, Q., Zheng, H., Zheng, M., Yan, Y., Liu, D., Ding, S., Zhao, D., Shen, G., Zhao, T., Qi, S., 2020. The moving of high emission for biomass burning in China: View from multi-year emission estimation and human-driven forces. Environ Int 142, 105812.

Xu, J., Wang, Q., Deng, C., McNeill, V.F., Fankhauser, A., Wang, F., Zheng, X., Shen, J., Huang, K., Zhuang, G., 2018. Insights into the characteristics and sources of primary and secondary organic carbon: High time resolution observation in urban Shanghai. Environ Pollut 233, 1177-1187.

Young, S.A., Cutten, D.R., Lynch, M.J., Davies, J.E., 1993. Lidar-Derived Variations in the Backscatter-to-Extinction Ratio in Southern-Hemisphere Coastal Maritime Aerosols. Atmos Environ a-Gen 27, 1541-1551.

Zarzycki, C.M., Bond, T.C., 2010. How much can the vertical distribution of black carbon affect its global direct radiative forcing? Geophysical Research Letters 37, n/a-n/a.

Zhang, L., Qiao, L., Lan, J., Yan, Y., Wang, L., 2020. Three-years monitoring of PM2.5 and scattering coefficients in Shanghai, China. Chemosphere 253, 126613.

Zhao, H., Mao, J.D., Zhou, C.Y., Gong, X., 2018. A method of determining multi-wavelength lidar ratios combining aerodynamic particle sizer spectrometer and sun-photometer. Journal of Quantitative Spectroscopy & Radiative Transfer 217, 224-228.

Zhao, L., Wang, W., Hao, T., Qu, W., Sheng, L., Luo, C., An, X., Zhou, Y., 2020. The autumn haze-fog episode enhanced by the transport of dust aerosols in the Tianjin area. Atmospheric Environment 237.

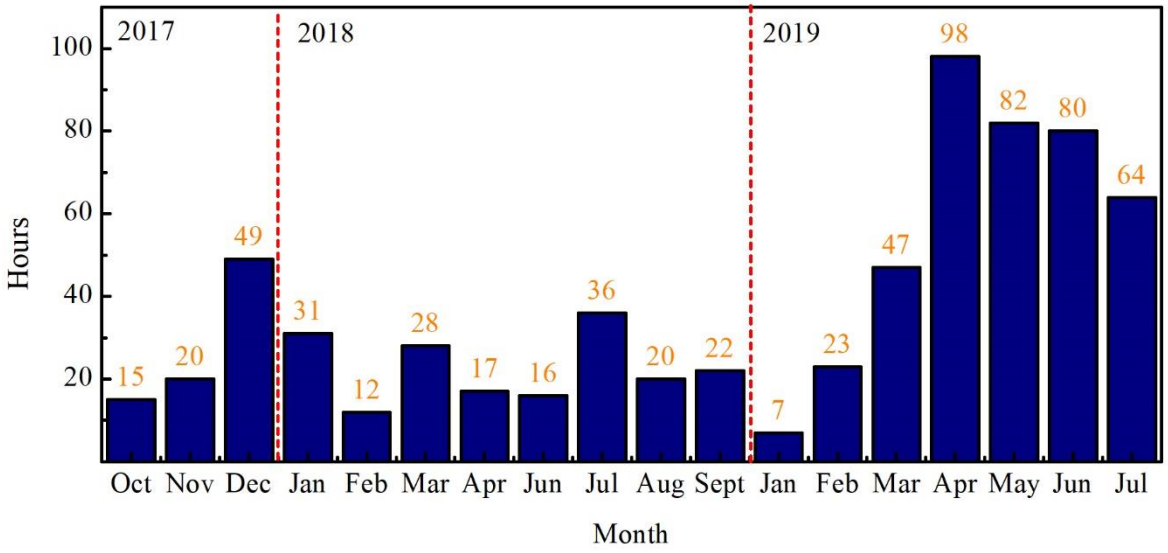

575 **Figure 1: Effective observation hours per month from 2017 to 2019.**

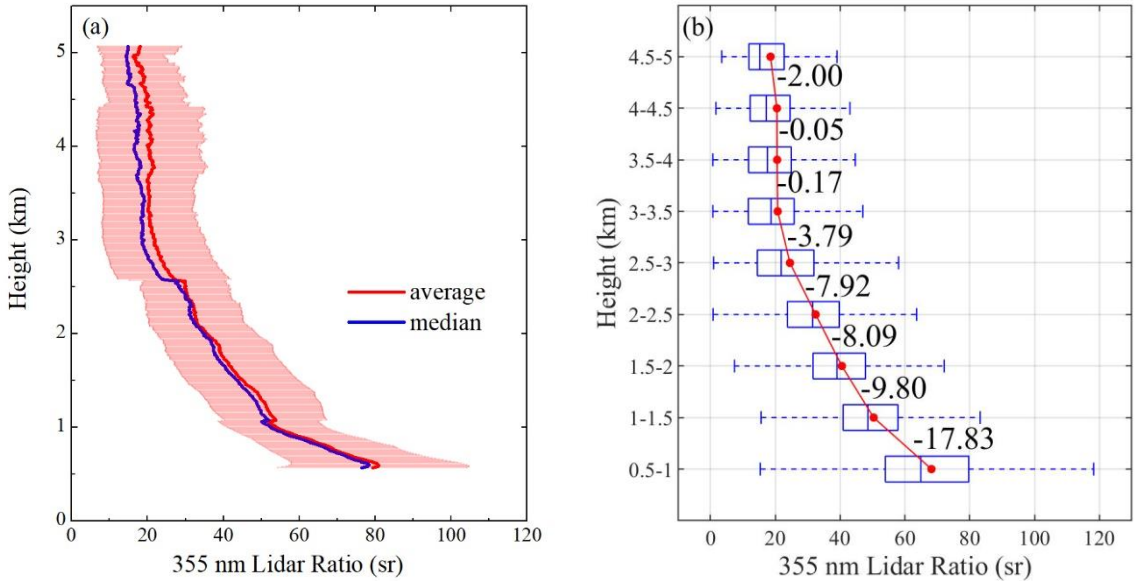

580 **Figure 2: General variation of LR. (a) Average profile of LR. The red line is the mean profile, the blue line is the median profile, and the red shadow is the error bar, indicating the standard deviation; (b) Average LR in different altitude range. The red line is a line of average values at different heights. The number between two points are the slopes between the two points.**

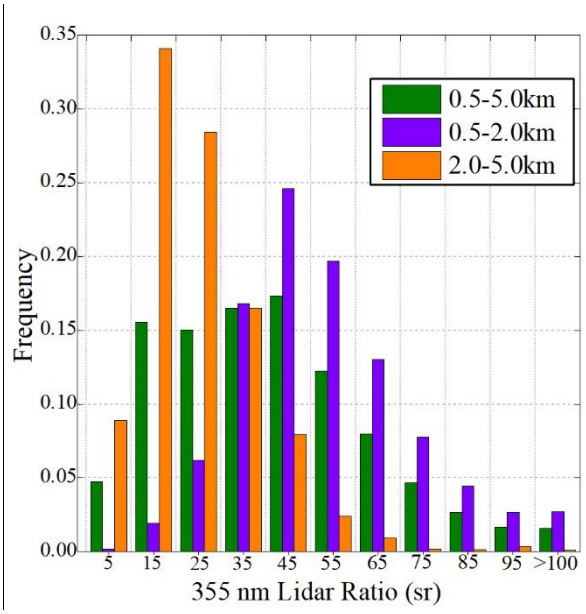

Figure 3: LR frequency distribution.

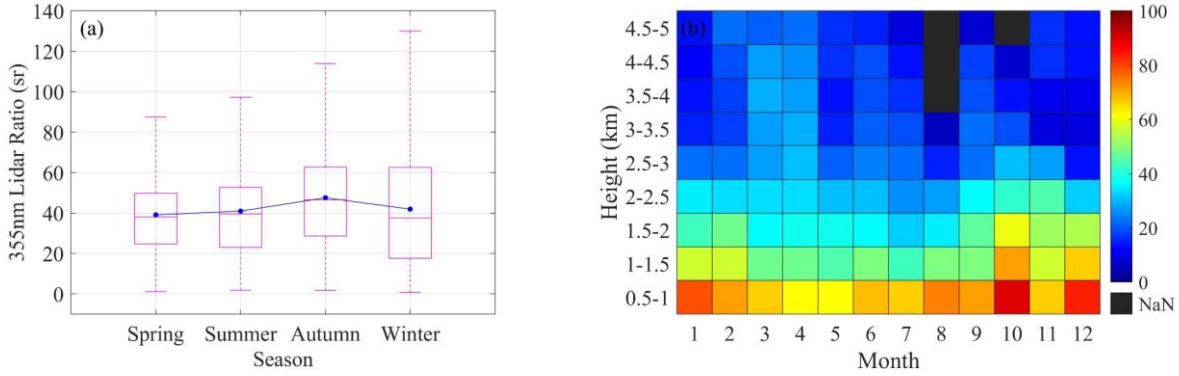

Figure 4: LR temporal variations. (a) Seasonal variations of LR. The blue dots are the average for each season; (b) Average of LR at different altitudes in different months. The black areas indicate invalid value.

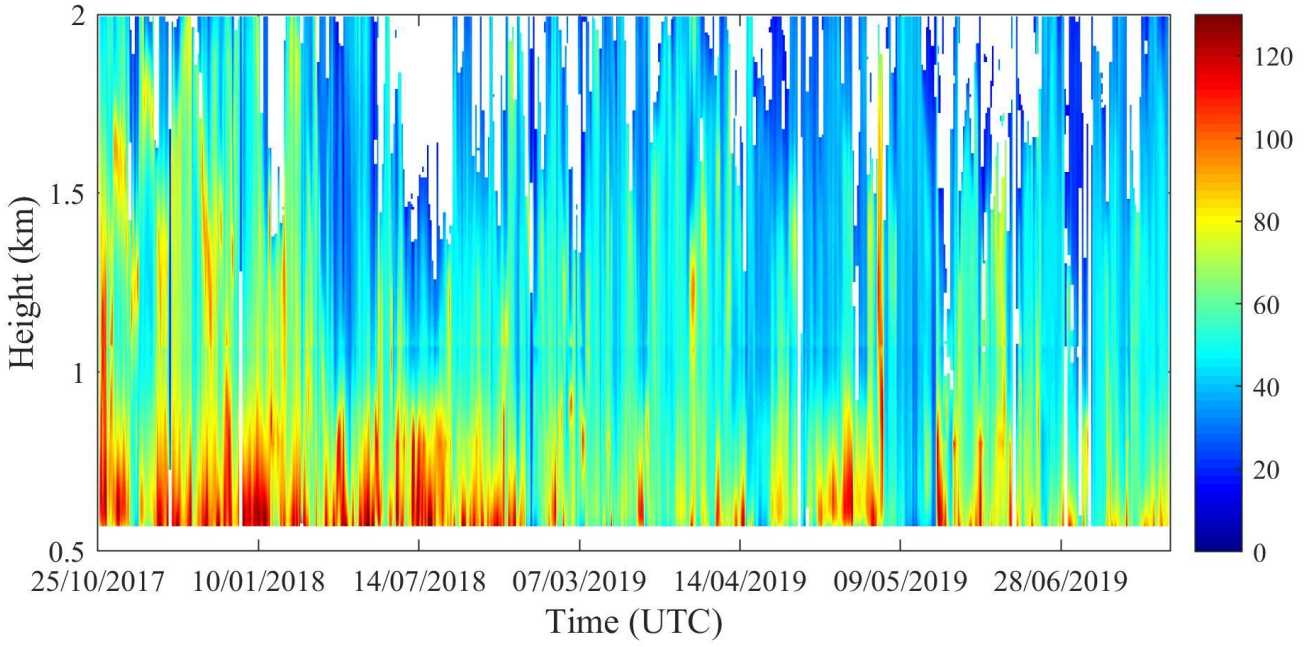

590 **Figure 5: The average LR of effective observation hours. The white areas indicate invalid values.**

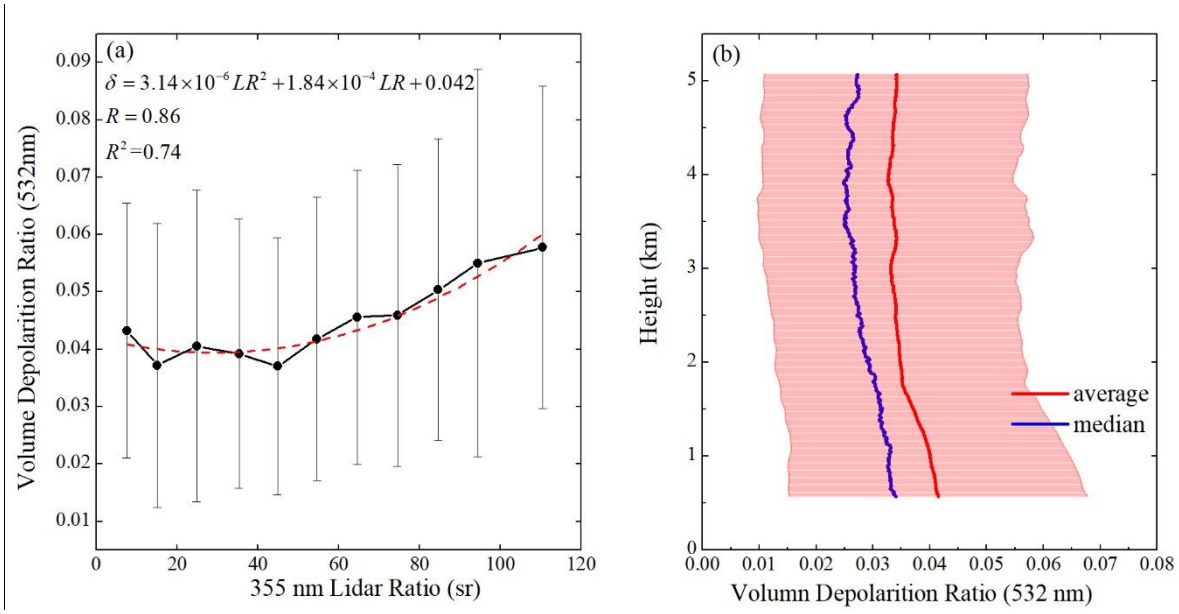

Figure 6: Effect of δ on LR. (a) LR was divided into 11 intervals and the mean value of δ in each interval was calculated. The dot and error bar represent the mean and standard deviation of δ in each interval. The red dotted line is the fitting line of LR and δ; (b) The red line is the mean profile of δ, the blue line is the median profile of δ, and the red shadow is the error bar, meaning
595 **the standard deviation.**

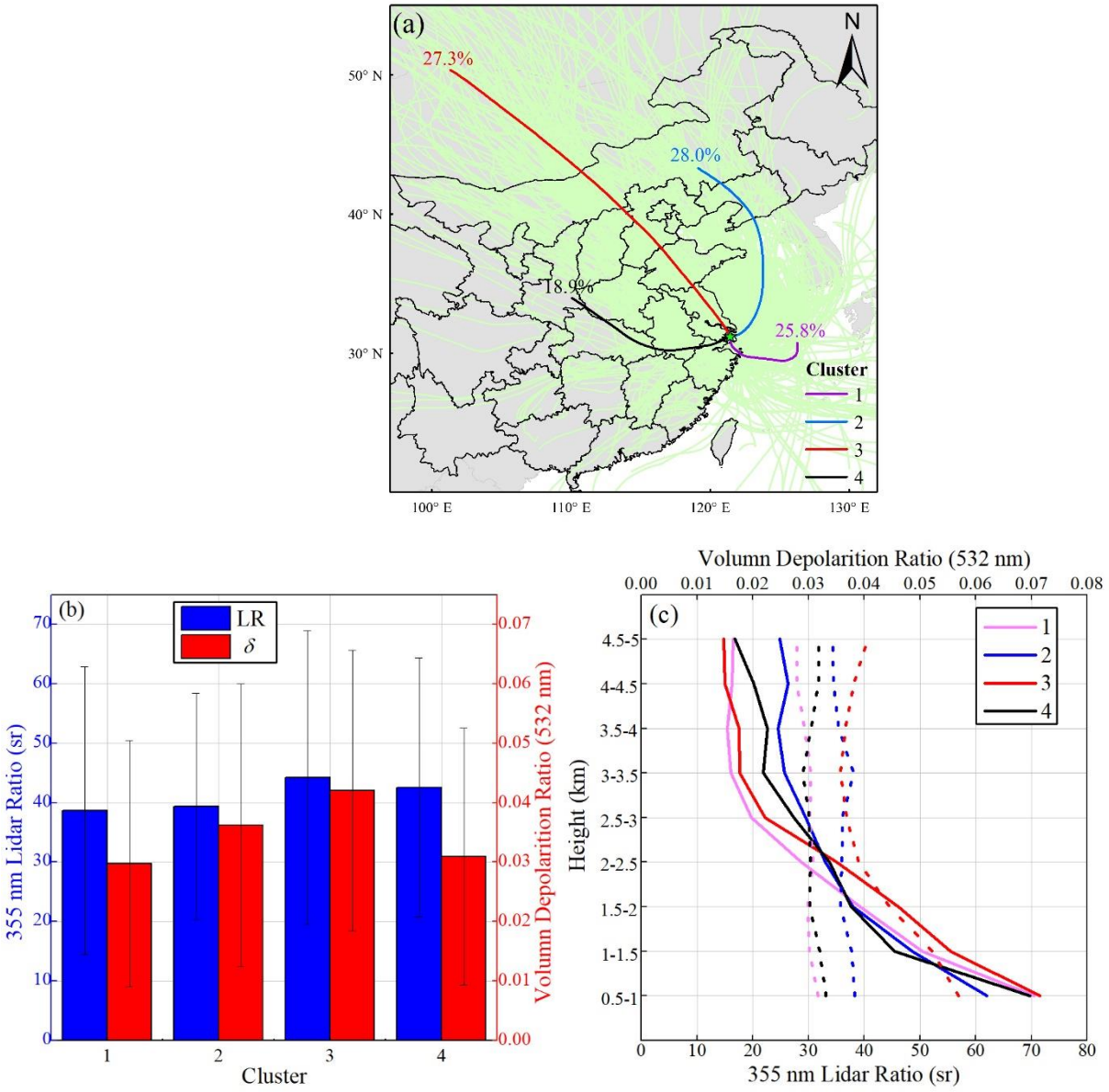

Figure 7: (a) 72-h back trajectory cluster analysis; (b) Mean values of LR and δ corresponding to different air masses; (c) The average of LR and δ at different heights corresponding to different air masses, the solid line is LR, the dotted line is δ.

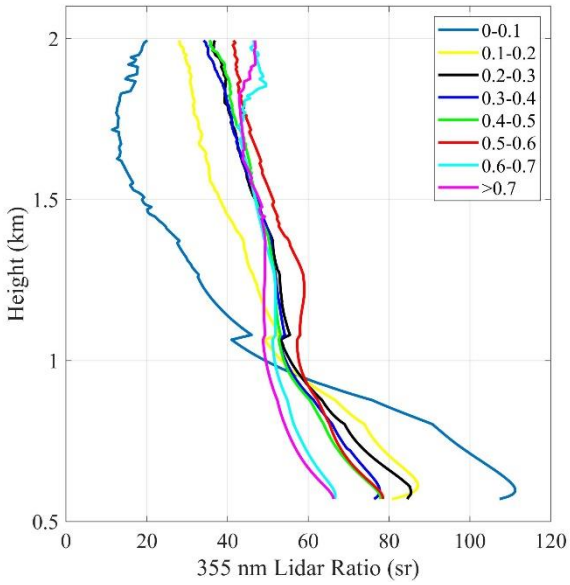

Figure 8: LR profiles in different AOD intervals.

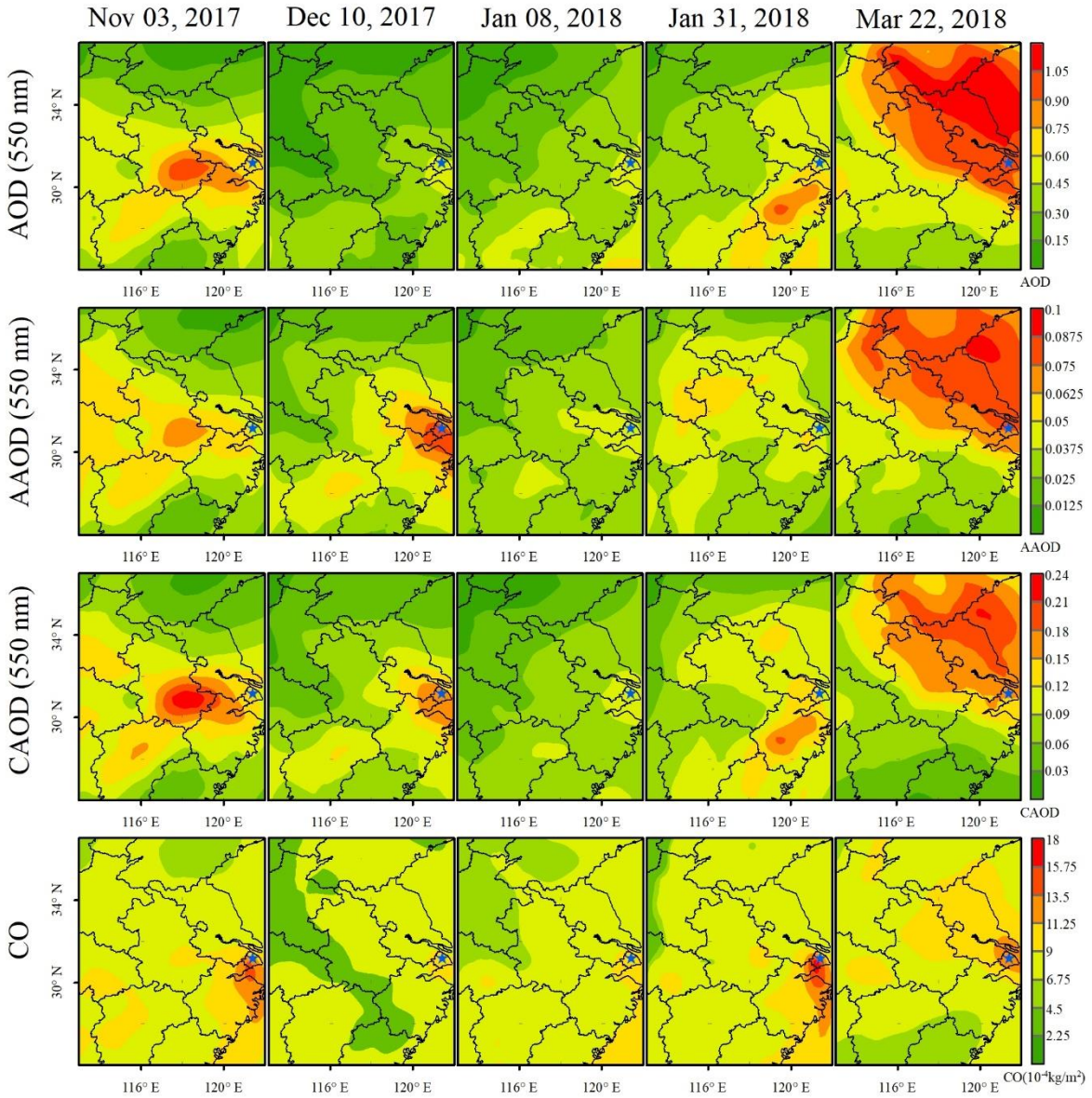

Figure 9: Spatial distribution of AOD, AAOD, CAOD and CO column concentrations in 5 cases. From left to right, different cases are represented, and from top to bottom, different tracers are represented. The blue star is the location of the Raman lidar.

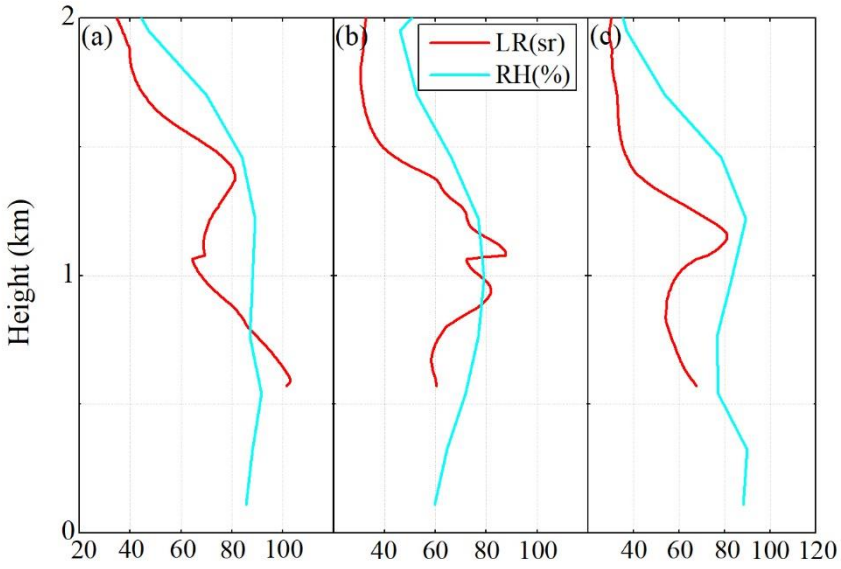

605

Figure 10: RH and LR profiles at the same time. (a) December 8, 2017, 20:00; (b) March 17, 2018, 16:00; (c) September 23, 2018, 20:00.